

# TESS Asteroseismic Predictions for Red Giants using Machine Learning

M. Schofield<sup>1,2★</sup>, G. R. Davies<sup>1,2</sup>, W. J. Chaplin<sup>1,2</sup>, A. Miglio<sup>1,2</sup>

<sup>1</sup>Department of Physics and Astronomy, the University of Birmingham, Birmingham B15 2TT, UK

<sup>2</sup>Stellar Astrophysics Centre (SAC), Department of Physics and Astronomy, Aarhus University, Ny Munkegade 120, DK-8000 Aarhus C, Denmark

Last updated 2017 May 31; in original form 2017 May 31

## ABSTRACT

For the first time, a classifier was used as a way to select solar-like asteroseismic targets before a future mission. The classifier managed to identify the detectable solar-like oscillations inside *Kepler* Red Giants with a 0.98% precision. To do this, it used only the global parameters  $[\log(g), \pi, T_{\text{eff}}, [\text{M}/\text{H}], I_{\text{mag}}]$ .

The same classifier was also used on the *Kepler* stars after they had been degraded into TESS-like observations. The classifier scored 0.86% and 0.74% when made to look like 1-year and 27-days of TESS-like data, respectively. This classifier could be used to select asteroseismic targets for TESS in the Continuous Viewing Zone (Ricker et al. 2014), and as a way of investigating any target selection bias in previous missions such as K2 and CoRoT.

## 1 INTRODUCTION

- We use a classifier to make detectability predictions for TESS (Ricker et al. 2014)
- Mention the application to PLATO (Rauer et al. 2014).
- Supervised classifiers have been used to determine the evolutionary state of variable stars: Debosscher et al. (2007), Sarro et al. (2009), Nun et al. (2014), Elorrieta et al. (2016). Similarly, unsupervised classifiers (Valenzuela & Pichara 2018) and regression (Ness et al. 2015) have also been used to determine evolutionary stages.
- Similarly, a neural network has been used to identify the evolutionary stage of Red Giant stars (Hon et al. (2017), Hon et al. (2018)).
- Machine learning has also been used to calculate stellar parameters (Bellinger et al. 2016), including oscillation frequencies (Davies et al. 2016).
- One reason to use Machine Learning for target selection is that it can reverse-engineer target selection bias, for example in K2 (Lund et al. 2015) and CoRoT (Baglin et al. 2006). This can provide insights into the formation history of the galaxy: Thomas et al. (2017)
- Summarise the Chapters.

## 2 THE DATASET

The data to perform Machine Learning on are the 1000 *Kepler* Red Giants from Davies et al. (in prep). These are shown in Figure 1. Machine Learning performs best when a large dataset is available to train the algorithm on. In order to increase the size of the dataset above 1000, the magnitude of each *Kepler* star was perturbed. Each star had its apparent magnitude perturbed 100 times.

The noise functions of *Kepler* and TESS were used as PDFs to draw apparent magnitudes from. These were used because they provide realistic distributions of the number of stars at different

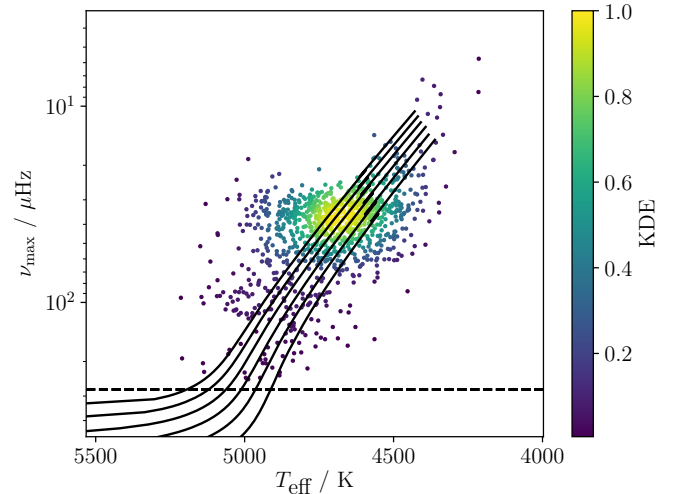


**Figure 1.** The 1000 *Kepler* Red Giants from Davies et al. (in prep). The colourbar shows the relative density of points with Kernel Density Estimation. The evolutionary tracks range from 0.9-1.5  $M_{\odot}$ .

magnitudes that the satellites observed/will observe. Many more fainter stars are observed than brighter stars because the volume of space that contains stars increases as the distance of observation increases.

The noise function of *Kepler* depends on the *Kepler* magnitude of the star,  $K_p$ . This noise function is from Chaplin et al. (2011). It is given by

$$\sigma = \frac{10^6}{c} \times \sqrt{c + 9.5 \times 10^5 \left( \frac{14}{K_p} \right)^5}, \quad (1)$$

where

$$c = 1.28 \times 10^{0.4(12-K_p)+7}. \quad (2)$$

The equivalent TESS noise function was estimated by calculating stellar shot noise, the noise from background stars, the read-out noise and the systematic noise. These four noise sources were then summed in quadrature to give the total TESS noise.

The *Kepler* and TESS noise functions were used as the PDFs to draw stellar magnitudes from. 100 magnitudes were drawn for every *Kepler* Red Giant. After removing gaps in the data, this left 60,000 samples. The lightcurves of this much larger *Kepler* dataset were then degraded to look like TESS observations.

### 3 MODIFYING *Kepler* DATA TO LOOK LIKE TESS

Before a classifier could be used on the Red Giant sample, the time-series data from *Kepler* needed to be adjusted for a different satellite and mission. These adjustments were made in the time domain before the signal was converted to the frequency domain.

Several different adjustments needed to be made to the *Kepler* data. One difference between the missions is the length of observation. The *Kepler* mission observed for 4 years, while TESS' nominal 2 year mission will observe stars for between 27 days to 1 year, according to the stars ecliptic latitude (Ricker et al. 2014).

As well as reducing the dataset length, the bandpass of observation needed to be adjusted. TESS will observe in a much redder bandpass than that of *Kepler*. This has the effect of reducing the amplitude of stellar signals (i.e the signals due to stellar granulation and solar-like oscillations), while leaving the white noise component unaltered (Ballot et al. 2011). Campante et al. (2016) found this bandpass correction to be 0.85 for TESS.

Thirdly, the noise level for a given star in *Kepler* is lower than the noise level in TESS. The noise level for the *Kepler* satellite depends on the *Kepler* magnitude of the star, equation 1. Noise from TESS was calculated for each star and added to the timeseries (c.f Section 2).

These three adjustments - the length of observation, the bandpass, and the noise level - were performed in the time domain. From the original *Kepler* timeseries, these adjustments were made:

- (i) Apply a  $4\sigma$  clip to the dataset to remove spurious points.
- (ii) Cut the 4 years of data down to the reduced dataset length with the shortest total length of gaps in the data.
- (iii) Adjust the bandpass by multiplying the flux by 0.85.
- (iv) Add noise from TESS by multiplying the predicted noise level by a random number from the standard normal distribution before adding to the signal.
- (v) Use the Lomb-Scargle periodogram to convert the signal from the time to frequency domain.

Examples of the TESS-like power spectra are shown in Figures 2 and 3. Power spectra were generated for the original 4-year *Kepler* sample, 1 year of TESS observations and 27 days of TESS observations. Once the timeseries had been made to look like TESS observations, a detection test was then run on the radial modes of every star in these 3 datasets.

### 4 DETECTION TEST

Section 3 described the method to transform the *Kepler* lightcurves into TESS-like power spectra. A detection test was then run on the

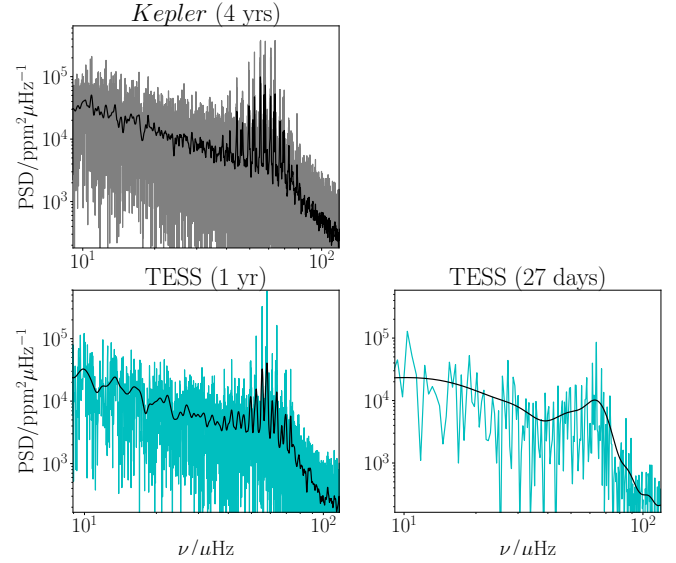


**Figure 2.** The Power spectra of KIC 9535399 is plotted three times with moving medians in black. The original Power Spectra is plotted in grey. The power spectra after making the data look like TESS are plotted in blue. The subplot on the bottom left shows 1 year of TESS observation (the maximum). The subplot on the bottom right column shows 27-days (the minimum).

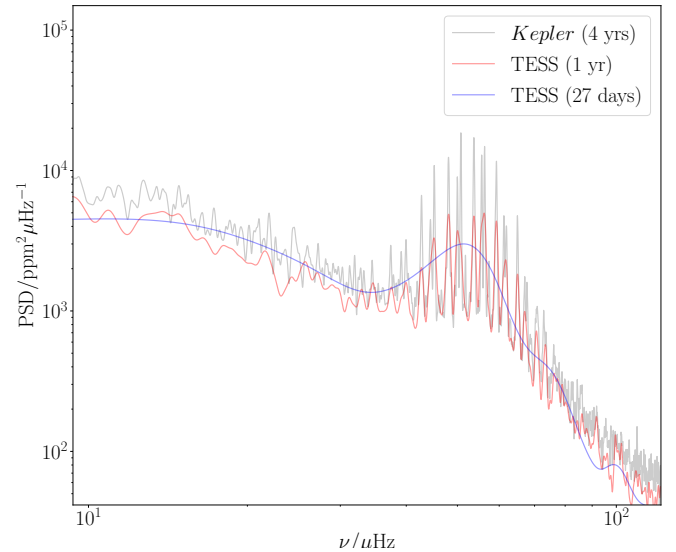


**Figure 3.** The Power Spectra of KIC 6768319. The original power spectra is in grey. The data was transformed into 1 year and 27 days of TESS observation. The moving median of these transformations are overlotted.

stars to determine which modes were visible after observation by TESS, and which were not.

First, a moving median was used to estimate the proportion of the signal that was due to white noise and stellar granulation. The solar-like mode envelope width was used as the frequency range of the moving median. This envelope width was calculated as

$$\Gamma_{\text{env}} = 0.66 \nu_{\text{max}}^{0.88}, \quad (3)$$

from Mosser et al. (2012). The moving median was used to inter-

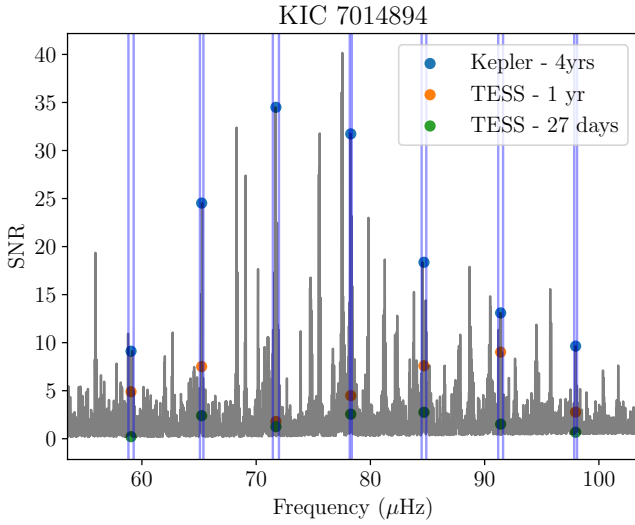


**Figure 4.** The SNR spectrum of KIC 7014894 after background subtraction. The SNR values of the radial modes in the star were extracted from this spectrum. The highest SNR value within the linewidth of each mode is taken to be the SNR value of that mode. The mode linewidths are shown as blue lines. The values of every mode in the original Kepler spectrum are plotted as blue points. The overplotted orange points are the SNR values after degrading the signal to 1 year of TESS observation. Similarly, the green points are the SNR values of 27 days of TESS observations. The white noise level and reduced observation time severely reduce the SNR of TESS observations compared to *Kepler*.

polate between frequencies in the power spectrum. It provided an estimate of the background  $B$  in the power spectrum ( $\text{ppm}^2\mu\text{Hz}^{-1}$ ). This background was divided out of the power  $P$  ( $\text{ppm}^2\mu\text{Hz}^{-1}$ ) in the power spectrum to get Signal-to-Noise ratio of the spectrum,

$$\text{SNR} = P/B. \quad (4)$$

Once the SNR spectrum for the star was recovered, the SNR values at the mode frequencies were extracted. To ensure the correct SNR values of every mode were used, a window was fitted around each peak-bagged mode frequency. The size of the window was given as the linewidth of the mode. The highest value in the window was taken as the SNR of the mode. An example of this for KIC 7014894 is shown in Figure 4.

Once all mode SNR values for the star were calculated, a detection test from (Chaplin et al. 2011) was run on each mode. This is described below.

The probability  $P$  that the SNR value of a solar-like mode of oscillation lies above some threshold  $\text{SNR}_{\text{thresh}}$  is

$$P(\text{SNR} \geq \text{SNR}_{\text{thresh}}) = p. \quad (5)$$

A false-alarm probability  $p$  of 5% was set; there is a 95% chance that the signal is due to solar-like oscillations, rather than noise. Equation 5 is solved for  $\text{SNR}_{\text{thresh}}$  by substituting  $P$  with

$$P = \int_x^\infty \frac{e^{-x}}{\Gamma(N)} x^{N-1} dx. \quad (6)$$

$N$  is the number of frequency bins that the mode occupies. The linewidth of each mode was used as the value of  $N$  in equation 6.

$\Gamma(N)$  is the Gamma function. The lower bound of Equation 6

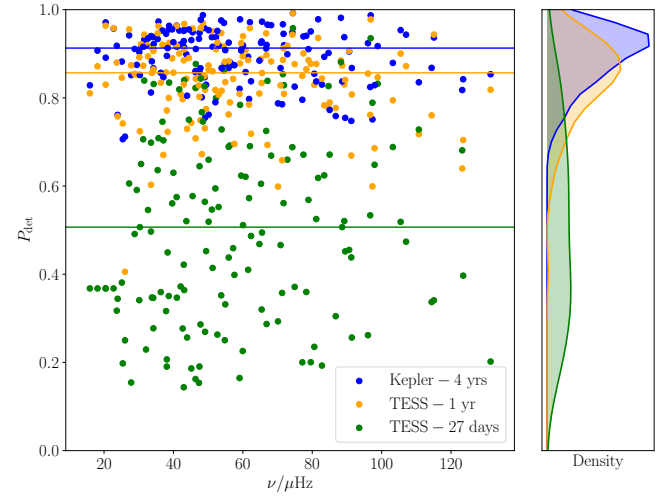


**Figure 5.** A plot showing the result of the detection test, after running on every mode in 20 stars. The results of the original power spectra are plotted in blue. The results of 1 year of TESS observation are in orange. 27 days of TESS observation is in green. At this short an observation, detecting individual modes will be extremely difficult.

is set to  $x = 1 + \text{SNR}_{\text{thresh}}$ . The noise in the  $N$  bins is assumed to follow  $\chi^2$   $2n_{\text{bins}}$  d.o.f statistics.

Once  $\text{SNR}_{\text{thresh}}$  is found, Equation 6 is solved again. This time it is solved for  $P$  by setting  $x = (1 + \text{SNR}_{\text{thresh}})/(1 + \text{SNR})$ . Here, SNR is the observed Signal-to-noise Ratio calculated from Equation 4. This calculates the probability that the frequency spike was due to stochastic excitation in the convective envelope of the star.

This detection test was applied to every mode of every star in the sample. Figure 5 shows the mode detection probabilities from this test for the original *Kepler* dataset, for 1-year of TESS observation and for 27 days of TESS observation. After the  $P_{\text{det}}$  values for the 3 datasets were calculated, a classifier was used to see if these results could be predicted rather than calculated. This is described in Section 5.

## 5 CLASSIFICATION

Section 3 describes how the lightcurves of every star were treated before a detection test was run on the oscillations in Section 4. After this, a random forest classifier was used to predict the detection probability of the modes in the Red Giants.

Classification algorithms work by assessing similarity<sup>1</sup>. In Classification, the training set is separated into groups based on the similarity of the data. The more information that was gained by splitting the data, the better. The data continues to be split until a prediction can be made (in this case about the detection probabilities of 3 radial modes [ $P_{\text{det}}(1)$ ,  $P_{\text{det}}(2)$ ,  $P_{\text{det}}(3)$ ]). In Decision Tree Classification, this is done once.

Here, a random forest classifier was used. This is made up of many independent Decision Trees which have been weighted to

<sup>1</sup> <http://www.simafore.com>

| KIC     | Iteration | $\log(g)$ | $\pi$ | $T_{\text{eff}}$ | [M/H] | $I_{\text{mag}}$ |
|---------|-----------|-----------|-------|------------------|-------|------------------|
| 9205705 | 1         | 2.758     | 0.688 | 4685             | -0.39 | 9.89             |
| 9205705 | 2         | 2.758     | 0.688 | 4685             | -0.39 | 9.19             |
| 9205705 | 3         | 2.758     | 0.688 | 4685             | -0.39 | 9.79             |
| 9205705 | 4         | 2.758     | 0.688 | 4685             | -0.39 | 11.30            |
| ...     |           |           |       |                  |       |                  |
| 9205705 | 100       | 2.758     | 0.688 | 4685             | -0.39 | 7.81             |
| 2554924 | 1         | 2.799     | 0.969 | 4594             | 0.27  | 8.46             |
| 2554924 | 2         | 2.799     | 0.969 | 4594             | 0.27  | 9.26             |
| ...     |           |           |       |                  |       |                  |

**Table 1.** An example of the X-dataset for 1 year of TESS-like observations. Every star has its magnitude perturbed 100 times. See Table 2 for the equivalent Y-dataset.

predict  $[P_{\text{det}}(1), P_{\text{det}}(2), P_{\text{det}}(3)]$ . Section 5.1 will explain how the data was prepared before the random forest classifier was used.

### 5.1 Preparing the data

Firstly, the detection probabilities of every mode were taken from Section 4. Each probability was put into a discrete bin (or *class*) depending on how likely the mode is to be detected. These discrete classes are given in equation 7.

$$P_{\text{det}} = \begin{cases} 2 & \text{if } 1.0 \geq P_{\text{det}} > 0.9, \\ 1 & \text{if } 0.9 \geq P_{\text{det}} > 0.5, \\ 0 & \text{if } 0.5 \geq P_{\text{det}} > 0.0. \end{cases} \quad (7)$$

Using equation 7, every mode was assigned a discrete class [0, 1 or 2], depending on how high the probability of detection was for that mode. The same three radial modes (3 *features*) were used for every star: the mode closest to the centre of the power-excess due to solar-like oscillations  $\nu_{\text{max},n}$ , the radial mode one overtone below that  $\nu_{n-1}$ , and one overtone above that,  $\nu_{n+1}$  [ $P_{\text{det}}(1)$ ,  $P_{\text{det}}(2)$ ,  $P_{\text{det}}(3)$ ]. It was important to use the same information for every star so that the algorithm could be trained on the patterns between the variables.

A classifier is an algorithm that can learn a relationship between variables. The classifier will map from some initial information about the star (the X data), to some unknown information (the Y data). In this work, the X data features were magnitude ( $K_p$  or  $I_{\text{mag}}$ ),  $\log(g)$ ,  $\pi$ ,  $T_{\text{eff}}$  and [M/H].  $\log(g)$ ,  $T_{\text{eff}}$  and [M/H] values are from Pinsonneault et al. (2014),  $\pi$  is from Gaia Collaboration et al. (2016) and  $I_{\text{mag}}$  is from Høg et al. (2000).

The Y data features were the  $P_{\text{det}}$  values of 3 radial modes, centred around  $\nu_{\text{max}}$ . An example of the final dataset for 1 year of TESS-like observations are shown in Tables 1 and 2.

### 5.2 Target selection using a classifier

The 60,000 samples were separated into a training dataset, and a testing set. 70% of the samples were used to train the classifier (46,410 stars); 30% of the stars were used to test the algorithm (19,890 stars). To train the classifier, the X and Y data in the training set was given to the algorithm ( $X_{\text{train}}$  and  $Y_{\text{train}}$ ). Once the classifier had been trained, the X data from the testing set was given to it ( $X_{\text{test}}$ ). The classifier then predicted a set of Y data for the testing set ( $Y_{\text{pred}}$ ). This was compared to the actual Y data for the testing set ( $Y_{\text{test}}$ ). The more similar  $Y_{\text{pred}}$  is to  $Y_{\text{test}}$ , the better the classifier replicated the data.

| KIC     | Iteration | $P_{\text{det}}(1)$ | $P_{\text{det}}(2)$ | $P_{\text{det}}(3)$ |
|---------|-----------|---------------------|---------------------|---------------------|
| 9205705 | 1         | 1                   | 2                   | 2                   |
| 9205705 | 2         | 1                   | 2                   | 2                   |
| 9205705 | 3         | 1                   | 2                   | 2                   |
| 9205705 | 4         | 1                   | 2                   | 1                   |
| ...     |           |                     |                     |                     |
| 9205705 | 100       | 1                   | 2                   | 2                   |
| 2554924 | 1         | 2                   | 2                   | 2                   |
| 2554924 | 2         | 2                   | 2                   | 2                   |
| ...     |           |                     |                     |                     |

**Table 2.** An example of the Y-dataset for 1 year of TESS-like observations. Every star has its magnitude perturbed 100 times. White noise is then added to the timeseries and mode detection probabilities are calculated for 3 radial modes centred around  $\nu_{\text{max}}$ . Lastly, these probabilities are put into discrete classes [0, 1 or 2]. The radial mode closest to  $\nu_{\text{max}}$  is  $P_{\text{det}}(2)$ . See Table 1 for the equivalent X-dataset.

| Satellite     | $T_{\text{obs}}$ | Precision | Hamming loss |
|---------------|------------------|-----------|--------------|
| <i>Kepler</i> | 4 years          | 0.98      | 0.02         |
| TESS          | 1 year           | 0.86      | 0.07         |
| TESS          | 27 days          | 0.74      | 0.25         |

**Table 3.** Results of the classifier on the original *Kepler* dataset, and the 1-year and 27-day TESS datasets. The 'Precision' column gives the average weighted precision of the classifier across the 3 classes [0, 1, 2] and 3 features [ $P_{\text{det}}(1)$ ,  $P_{\text{det}}(2)$ ,  $P_{\text{det}}(3)$ ].

Two metrics were used to measure the performance of the algorithm. The first was the precision of the classifier, weighted across the classes [0, 1, 2] and the detection probability features  $P_{\text{det}}(1)$ ,  $P_{\text{det}}(2)$  and  $P_{\text{det}}(3)$ . This precision  $P$  is given as

$$P = t_p / (t_p + f_p), \quad (8)$$

where  $t_p$  are true-positives and  $f_p$  are false-positives. The classifier's precision is its ability to not label a negative sample as positive<sup>2</sup>.

The second was the Hamming loss<sup>2</sup> (Wegner 1960) of the algorithm. This was used to give another measure of similarity between the predicted  $P_{\text{det}}$  values  $Y_{\text{pred}}$ , and the testing  $P_{\text{det}}$  values  $Y_{\text{test}}$ :

$$H_{\text{loss}}(Y_{\text{test}}, Y_{\text{pred}}) = \frac{1}{n_{\text{classes}}} \sum_{j=0}^{n_{\text{classes}}-1} 1(Y_{\text{pred}} \neq Y_{\text{test}}). \quad (9)$$

A Hamming loss score of 0.0 means that  $Y_{\text{pred}}$  is identical to  $Y_{\text{test}}$ . A score of 1.0 means that there are no similar values between  $Y_{\text{pred}}$  and  $Y_{\text{test}}$ . Precision and Hamming loss are similar (but not identical) measures of the success of a classifier. By using both metrics, the usefulness of the classifier can be better assessed. The precision and Hamming loss of the classifier on the *Kepler* and TESS datasets are shown in Table 3.

The classifier was adjusted in order to improve the predictions made by the classifier on the *Kepler* and TESS datasets. This was done by varying Equation 7. It was varied by changing the number of classes and range of  $P_{\text{det}}$  values for each class. The number of classes was varied from 2 (i.e the mode was detected (1) or it was not (0)) to 6. The width of each bin was also varied to ensure that bins were not underpopulated. It was found that the 3 classes and

<sup>2</sup> <http://scikit-learn.org>

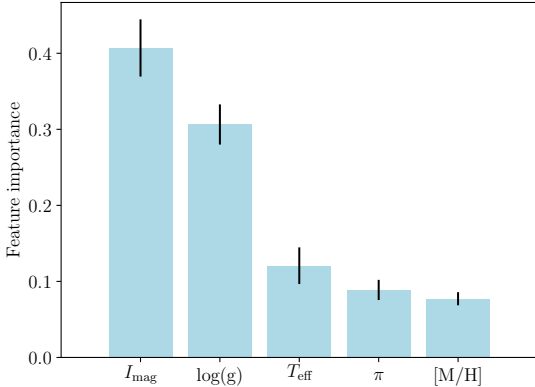


Figure 6. The feature importance of the 5 x-data columns.

$P_{\text{det}}$  ranges given in equation 7 gave the best predictions for the 3 *Kepler* and TESS datasets.

The results for the original *Kepler* dataset and for 1-year of TESS data are very good; the classifier was able to replicate the mode detection predictions of the stars in these cases. This means that a classifier can be used as a tool for target selection for future missions. Once the classifier predicted  $P_{\text{det}}$  values, the stars could be ranked from those with many detected modes, to those with the fewest. In this way, the classifier could be used as the target selection function of solar-like oscillators for TESS.

For the 27-day TESS dataset, the classifier was only able to correctly predict the  $P_{\text{det}}$  values of 74% of the modes. This is likely to be because with these TESS targets, the dataset is too short and the white noise level is too high for individual modes to be reliably detected. In this case, the classifier could not be expected to perform better. It is arguably no less reliable than a mode detection test, although it is much faster for large datasets.

### 5.3 Feature Importance

Here, a classifier was used to predict the detection probabilities of individual modes in *Kepler* Red Giant stars. As well as being much faster than a conventional mode detection test, an added bonus of the classifier method is that it returns the ‘feature importance’ of each column in the x-data.

As Table 1 shows, the x-data features that are given to the classifier are  $[\log(g), \pi, T_{\text{eff}}, [M/H], I_{\text{mag}}]$ . Some of these features are more important than others when predicting the detection probability of solar-like modes  $[P_{\text{det}}(1), P_{\text{det}}(2), P_{\text{det}}(3)]$ . The relative importance of these columns is known as the feature importance. This feature importance sums to 1.

The feature importances of the x-data columns are given in Figure 6. The feature with the highest influence on mode detectability is apparent stellar magnitude  $I_{\text{mag}}$ . This is not surprising: a higher value of  $I_{\text{mag}}$  will result in more  $\chi^2$  2 Degrees-of-Freedom white noise in the observation. This will make oscillations less likely to be detected above the white noise background.

After the apparent stellar magnitude, surface gravity  $\log(g)$  also has a heavy influence on  $P_{\text{det}}$  value. This is because  $\log(g)$  is a proxy for the central frequency of the solar-like mode envelope  $\nu_{\text{max}}$  ( $\nu_{\text{max}} \propto \log(g)$ ). As a star evolves from the Main-Sequence and up the Red Giant Branch, the radius of the star increases. This

decreases the  $\log(g)$  and  $\nu_{\text{max}}$  values of the star. Kjeldsen & Bedding (1995) showed that oscillation amplitude is proportional to bolometric luminosity divided by mass ( $A_{\text{osc}} \propto L/M$ ). As a star evolves ‘up’ the Hertzsprung-Russell diagram, its bolometric luminosity increases while its mass stays roughly the same. This leads to larger oscillation amplitudes which are more likely to be detected. Mathur et al. (2011) also gives a good explanation of how the granulation properties (and hence the oscillation profile) change as a star evolves.

Comparatively, effective temperature  $T_{\text{eff}}$  is less useful than  $\log(g)$  when predicting detection probability. It is less closely tied to the oscillation properties of the star than  $\log(g)$ , although it is a property used to estimate  $\nu_{\text{max}}$  with the scaling relations (Chaplin et al. 2011).

Lastly, parallax  $\pi$  and metallicity  $[M/H]$  are the least strongly tied to the oscillation properties of these RG stars. Parallax is connected to apparent magnitude and  $T_{\text{eff}}$  and  $[M/H]$  is connected to  $\log(g)$ . The feature importances of  $T_{\text{eff}}$ ,  $\pi$  and  $[M/H]$  highlight the additional information that these values bring, as well as indirectly through  $I_{\text{mag}}$  and  $\log(g)$ .

### 5.4 Comparing results between different evolutionary states

So far in this paper, the evolutionary state of the Red Giant population from Davies et al. (in prep) has been ignored when predicting mode detection probability  $P_{\text{det}}$ . In reality, the 1000 *Kepler* Red Giants used in this work are a mixture of Red Giant Branch (RGB), Red Clump (RC) and Secondary Clump (2CL) stars. This Section investigates whether there is any difference in the predictions if the stars are first separated into RGB, RC and 2CL groups. The evolutionary states of the stars in the sample were taken from Elsworth et al. (2017).

If a Red Giant Branch is massive enough, it will undergo the Helium flash and become a Red Clump star. Red Clump stars are Helium-core burning stars, and all have very similar core masses to each other. These stars have very different  $g$ -mode period spacings to RGB stars, but are otherwise difficult to differentiate (Chaplin & Miglio (2013), Bedding (2011), Beck et al. (2011)). If a star is more massive than  $\approx 1.8M_{\odot}$ , it will instead become a Secondary Clump star. This means that it will undergo Helium-core burning without the Helium flash.

The Red Giant dataset was separated into 3 subsets; the RGB, RC and 2CL stars. Each subset was treated in the same way as in Table 3. Table 4 gives the full list of results when the RGB, RC and 2CL stars are separated.

Table 4 shows that there is a negligible difference in predictions between stars undergoing Helium-core burning (RC and 2CL stars) and those that are not (RGB stars). This leads to the conclusion that a classifier can predict the mode detectability of Red Giants at different evolutionary states equally well. It is therefore not necessary to separate out these stars into different evolutionary states before predicting  $P_{\text{det}}$ .

## 6 CONCLUSION

1000 peak-bagged *Kepler* Red Giant stars from Davies et al. (in prep) were used to determine whether asteroseismic target selection could be done using a classifier. Rather than using Machine Learning to determine the evolutionary state of these stars, a classifier was instead used to predict which individual solar-like oscillations



| Evolution | Satellite     | $T_{\text{obs}}$ | Precision | Hamming loss |
|-----------|---------------|------------------|-----------|--------------|
| RGB       | <i>Kepler</i> | 4 years          | 0.98      | 0.03         |
| RGB       | TESS          | 1 year           | 0.83      | 0.16         |
| RGB       | TESS          | 27 days          | 0.75      | 0.25         |
| RC        | <i>Kepler</i> | 4 years          | 0.96      | 0.04         |
| RC        | TESS          | 1 year           | 0.90      | 0.09         |
| RC        | TESS          | 27 days          | 0.77      | 0.24         |
| 2CL       | <i>Kepler</i> | 4 years          | 0.97      | 0.03         |
| 2CL       | TESS          | 1 year           | 0.83      | 0.14         |
| 2CL       | TESS          | 27 days          | 0.69      | 0.30         |

**Table 4.** Results of the classifier when RGB, RC and 2CL stars are separated. Results are shown when the data are treated like *Kepler* stars, and when they are degraded to look like 1-year and 27-day TESS observation. The ‘Precision’ column gives the average weighted precision of the classifier across the 3 classes [0, 1, 2] and 3 features [ $P_{\text{det}}$  (1),  $P_{\text{det}}$  (2),  $P_{\text{det}}$  (3)].

inside the Red Giants could be detected with a future space mission. The mission in question here was TESS, although the same technique can be easily applied to other missions such as PLATO. This tool can also be used to understand target selection bias in previous missions, such as K2 and CoRoT.

Firstly, the number of samples was increased by perturbing stellar magnitudes 100 times for each star. These perturbed magnitudes were drawn from a PDF of the noise function (Section 2). After removing stars where global parameters or fitted modes were unavailable, this left 60,000 *Kepler* samples.

Once the number of samples was increased, the timeseries’ were degraded to transform them into TESS-like observations (Section 3). The dataset length was reduced, white noise was added to the signal, and the bandpass of observation was reddened. A moving median was calculated for the power spectra of these TESS-like Red Giants to estimate the total background in the signal. This was divided out of the spectra, leaving a Signal-to-Noise ratio at every frequency bin (equation 4).

A detection test was then run on the SNR values at every mode frequency (Section 4). This gave a detection probability  $P_{\text{det}}$  between 0.0 and 1.0 for every mode. In order to prepare the detection probabilities before Classification, each continuous  $P_{\text{det}}$  value was assigned a discrete class ([0,1 or 2]; equation 7).

A classifier was then given the global photometric and spectroscopic properties of the Red Giant sample, along with mode detection probabilities for each star. The parameters [ $\log(g)$ ,  $\pi$ ,  $T_{\text{eff}}$ ,  $[M/H]$ ,  $I_{\text{mag}}$ ] from APOKASC (Pinsonneault et al. 2014), TGAS (Gaia Collaboration et al. 2016) and Tycho2 (Høg et al. 2000) were the 5 X-data features. The  $P_{\text{det}}$  values of 3 radial modes centred around  $\nu_{\text{max}}$  were used as the Y-data features. The classifier used the global stellar parameters (the X-data) to make predictions about mode detectability (the Y-data). The stars with the largest number of detected modes could then be selected as the Red Giants for observation by TESS.

The classifier successfully made predictions about the original 4 years of Kepler data; the algorithm had a weighted precision 0.98 across the 3  $P_{\text{det}}$  features. This confirms the proof of concept that classifiers can be used as a way to select solar-like asteroseismic targets before future missions. As well as this, this shows that it can be used to investigate any possible target selection bias, for example in K2 or CoRoT. Classification vastly reduces the computation time required to produce a target selection function, especially when large datasets are involved ( $\geq 50,000$  stars).

Degrading the Red Giant data to make predictions for 1 year of

TESS observations was also successful. The predicted mode detections scored a weighted precision of 0.86 across the 3  $P_{\text{det}}$  features. This illustrates that Classification is a valid target selection method for TESS targets in the Continuous Viewing Zone (CVZ, (Ricker et al. 2014)).

Using the classifier on 27 days of TESS data returned detection predictions with a precision of 0.74. This is too low for the classifier to be used to select solar-like oscillators for 27 days of TESS observation. The precision is lower when stars are observed by TESS for 27 days because the white noise level is too high and the length of observation is too short to make robust predictions of individual solar-like oscillations. It may be that individual solar-like oscillations cannot be detected in 27 days of TESS data. If this is the case, then the classifier should not be expected to make robust detection predictions for these stars.

## REFERENCES

- Baglin A., et al., 2006. p. 3749, <http://adsabs.harvard.edu/abs/2006cosp...36.3749B>
- Ballot J., Barban C., van’t Veer-Menneret C., 2011, *Astronomy and Astrophysics*, 531, A124
- Beck P. G., et al., 2011, *Science*, 332, 205
- Bedding T. R., 2011, arXiv:1107.1723 [astro-ph]
- Bellinger E. P., Angelou G. C., Hekker S., Basu S., Ball W. H., Guggenberger E., 2016, *The Astrophysical Journal*, 830, 31
- Campante T. L., et al., 2016, preprint, 1608, arXiv:1608.01138
- Chaplin W. J., Miglio A., 2013, *Annual Review of Astronomy and Astrophysics*, 51, 353
- Chaplin W. J., et al., 2011, *The Astrophysical Journal*, 732, 54
- Davies G. R., et al., 2016, *Monthly Notices of the Royal Astronomical Society*, 456, 2183
- Debosscher J., Sarro L. M., Aerts C., Cuypers J., Vandenbusche B., Garrido R., Solano E., 2007, *Astronomy and Astrophysics*, 475, 1159
- Elorrieta F., et al., 2016, *Astronomy and Astrophysics*, 595, A82
- Elsworth Y., Hekker S., Basu S., R. Davies G., 2017, *Mon Not R Astron Soc*, 466, 3344
- Gaia Collaboration et al., 2016, *Astronomy and Astrophysics*, 595, A2
- Høg E., et al., 2000, *Astronomy and Astrophysics*, 355, L27
- Hon M., Stello D., Yu J., 2017, *Monthly Notices of the Royal Astronomical Society*, 469, 4578
- Hon M., Stello D., Yu J., 2018, *Monthly Notices of the Royal Astronomical Society*
- Kjeldsen H., Bedding T. R., 1995, *Astronomy and Astrophysics*, 293, 87
- Lund M. N., Handberg R., Davies G. R., Chaplin W. J., Jones C. D., 2015, *The Astrophysical Journal*, 806, 30
- Mathur S., et al., 2011, *The Astrophysical Journal*, 741, 119
- Mosser B., et al., 2012, *A&A*, 537, A30
- Ness M., Hogg D. W., Rix H.-W., Ho A. Y. Q., Zasowski G., 2015, *The Astrophysical Journal*, 808, 16
- Nun I., Pichara K., Protopapas P., Kim D.-W., 2014, *The Astrophysical Journal*, 793, 23
- Pinsonneault M. H., et al., 2014, *The Astrophysical Journal Supplement Series*, 215, 19
- Rauer H., et al., 2014, *Experimental Astronomy*, 38, 249
- Ricker G. R., et al., 2014, *Journal of Astronomical Telescopes, Instruments, and Systems*, 1, 014003
- Sarro L. M., Debosscher J., LÁspez M., Aerts C., 2009, *Astronomy and Astrophysics*, 494, 739
- Thomas A., Stevenson E., Gittins F. W. R., Miglio A., Davies G., Girardi L., Campante T. L., Schofield M., 2017. eprint: arXiv:1610.08862, p. 05006, doi:10.1051/epjconf/201716005006, <http://adsabs.harvard.edu/abs/2017EPJWC.16005006T>
- Valenzuela L., Pichara K., 2018, *Monthly Notices of the Royal Astronomical Society*, 474, 3259

Wegner P., 1960, [Commun. ACM](#), 3, 322

This paper has been typeset from a  $\text{\TeX}/\text{\LaTeX}$  file prepared by the author.